Combination of optical transitions of polarons with Rashba effect in methylammonium lead trihalide perovskites under high magnetic fields

Y. H. Shin,[1] Halim Choi,[1] C. Park,[1] D. Park,[2] M. S. Jeong,[2] H. Nojiri,[3] Z. Yang,[4] Y. Kohama,[4] and Yongmin Kim[1,*]

[1]*Department of Physics, Dankook University, Cheonan 31116, Korea*
[2]*Department of Physics, Hanyang University, Seoul 04763, Korea*
[3]*Institute for Materials Research, Tohoku University, Sendai 980-8577, Japan*
[4]*Institute for Solid State Physics, The University of Tokyo, Kashiwa 277-8581, Japan*

(Received 8 April 2021; revised 10 June 2021; accepted 7 July 2021; published 22 July 2021; corrected 28 July 2021)

We investigate photoluminescence (PL) transitions of MAPbX_3 (X = I, Br, and Cl) organic-inorganic hybrid perovskite single crystals under magnetic fields of up to 60 T. In these materials, sharp free-exciton transition peaks emerge at a low temperature (4.2 K). Under strong magnetic fields, the free-exciton PL transitions of three different halogens show dramatic differences. The free-exciton transitions of the $MAPbCl_3$ crystal undergo negative energy shifts, while those of the $MAPbBr_3$ crystal show normal diamagnetic shifts. To obtain the variation from Cl to Br, we attempt to measure PL transitions of $MAPbCl_xBr_{3-x}$. For $MAPbI_3$, the transition-energy shifts for both σ^+ and σ^- transitions at 4.2 K exhibit a power-law dependence on the magnetic field. Such inconsistent magnetic-field effects on different halogens make it difficult to understand the transition-energy behavior through a unified model. We propose a possible mechanism for the field effects that is based on a combination of the Rashba effect induced by strong spin-orbit coupling and the polaron effect caused by the polar nature of the inorganic elements.

DOI: 10.1103/PhysRevB.104.035205

I. INTRODUCTION

Organic-inorganic hybrid perovskites (OIHPs) of the form MAPbX_3 (X = I, Br, and Cl) have been intensively investigated due to their versatility for use in not only basic research but also industrial applications. Although vast investigations were initiated on $MAPbI_3$ because of its high solarcell efficiency of over 25% [1,2], band-gap engineering by substituting or mixing with other halogens (Br and Cl) made it possible to extend its applications to light-emitting as well as light-detection devices. However, even with the enormous potential for optoelectronic applications, the detailed physical characteristics of this material family remain unclear.

An indirect band alignment in the conduction and valence bands, which is necessary for a slow recombination rate, has been suggested, where the Rashba effect induced by the strong spin-orbit coupling (SOC) within its inorganic lattice framework plays an important role. The strong SOC of the Pb 6p orbital produces a large Rashba splitting in the conduction-band minimum at the R-point, whereas the weak SOC of the Pb 6s and halogen p orbitals yields a small Rashba splitting in the valence band. The large and small Rashba splittings are proposed to be responsible for indirect band alignment in MAPbX_3. The Rashba effect in OIHPs is an intriguing but challenging research subject. For example, the exciton fine structure has been investigated in $MAPbI_3$ nanocrystals. The excitonic state is known to split into ground singlet and excited triplet states due to the exchange interaction. The Rashba effect exchanges these states such that the triplet states become the ground state and the singlet states transform into a dark excited state [3–6]. Recently, it was suggested that dynamic and static Rashba effects could appear in bulk $MAPbBr_3$ and $CsPbBr_3$ crystals. The dynamic Rashba effect occurs inside bulk crystals due to the dynamic orientation of the MA^+ or Cs^+ cation in the inorganic cage. The effect disappears at low temperatures below 100 K for $CsPbBr_3$, whereas it persists below 100 K for $MAPbBr_3$. The static Rashba effect, on the other hand, emerges only on the surface of a bulk crystal and originates from the surface reconstruction through MA^+ cation ordering [7].

Due to the polar crystal characteristic of OIHPs, charge carriers interact with the phonons generated by the polar lattice, forming small and large polarons [8–11]. The polaron effects in OIHP are as complicated as their complicated structure. Both small and large polarons modify the effective mass and mobility of charge carriers because the carriers are localized near the polar lattice. It is generally known that the small and large polarons show an incoherent hopping and a bandlike transport behavior, respectively. The dynamic orientation of the organic cation (MA^+) that couples with excess charges causes the distortion of the inorganic octahedron, forming a small polaron [10,12,13]. Unlike the small polaron, in which the charge carriers are localized within several unit cells, the charge carriers in the bands, coupled with the longitudinal optical (LO) phonon caused by the inorganic lattice bonding, generate a large polaron [10,14–16]. The formation of the large polaron is due to the Pb-halide-Pb deformation modes and does not depend on the cation species (MA or Cs) [17]. Therefore, the substitution of halides is expected to be the origin of the difference in the character of the large polarons. OIHPs with different halogens have different bond

*Corresponding author: yongmin@dankook.ac.kr

polarities because of the electronegativity difference. The known Pauling electronegativities of inorganic elements in halide perovskites are 1.87 (Pb), 3.16 (Cl), 2.96 (Br), and 2.66 (I). For a polar covalent bond, the fraction of ionic bonding can be calculated by using the following simple equation:

$$\text{fraction of ionic bonding } (\%) = (1 - e^{-(\Delta x/2)^2}) \times 100, \quad (1)$$

where Δx is the electronegativity difference between the ionic elements, which are Pb and the halogen in OIHP. The calculated fractions of ionic bonding of the halide perovskites are 34.0% ($MAPbCl_3$), 25.7% ($MAPbBr_3$), and 14.4% ($MAPbI_3$). Such differences in the ionic bonding fraction of OIHPs may cause the polaron effects with the replacement of the halogen. Systematic Raman and infrared spectroscopy studies [18,19] reported that with the substitution of the halogen in the sequence of Cl, Br, and I, the vibrational frequencies of the OIHP undergo redshifts, which can be attributed to the reduction of the ionic bonding fraction. In Ref. [18], the authors found that irrespective of the MA cation species, element substitution in the sequence of Cl, Br, and I decreases all vibrational frequencies including stretching, bending, rocking, and torsion modes.

In this work, we report magnetophotoluminescence (MPL) transitions of $MAPbX_3$ (X = Cl, Br and I) single crystals under high magnetic fields of up to 60 T by using capacitor bank driven pulsed magnets and up to 19 T by using a superconducting dc magnet at 4.2 K. Optical transition measurement under magnetic fields is a powerful tool to determine various physical parameters of given materials, such as the dielectric constant, effective mass, g-factor, exciton Bohr radius, and/or exciton binding energy. Most previous works involving magnetoabsorption measurements under ultrahigh magnetic fields focused on the exciton Bohr radius and binding energy for OIHPs [20–23]. In the present study, we report that MPL transitions of free excitons (FX) strongly depend on the halogen in an inconsistent manner. For the $MAPbCl_3$ crystal, two FX transitions undergo spectral redshifts, and a new peak emerges above 20 T, which shows a blueshift as the magnetic field increases. For the $MAPbBr_3$ crystal, two FX transitions can be understood as ordinary diamagnetic energy shifts with a different diamagnetic coefficient obtained from magnetoabsorption measurements. To investigate the spectral difference between $MAPbCl_3$ and $MAPbBr_3$, we measured MPL transitions of $MAPbCl_xBr_{3-x}$ (x = 0.5, 1.0, 1.5, 2.0, and 2.5) crystals. For the $MAPbI_3$ crystal, the FX transition shows a power-law dependence on the magnetic field. Such unconventional optical transitions caused by the different halogens under magnetic fields are difficult to explain with one unified model and can be understood by the combination of the dynamic (bulk) Rashba and polaron effects.

II. EXPERIMENTAL SECTION

A. Sample preparation

All chemicals employed to grow samples were used as received without further purification. Methylammonium halides (CH_3NH_3X; X = Cl, Br, I) were sourced from Greatcell Solar Materials. Lead (II) halides (X = Cl, Br, I) were purchased from Alfa Aesar. Reagent-grade organic solvents such as γ-butyrolactone (GBL), dimethyl sulfoxide (DMSO), and dimethyl formamide (DMF) were purchased from Aldrich. $MAPbX_3$ [MA = $CH_3NH_3^+$ (methylammonium), $X = Cl^-$, Br^-, Cl^-] single crystals were prepared using the inverse temperature crystallization (ITC) method [24,25]. For the precursor solution, the equivalent molar ratio of MAX and PbX_2 was dissolved in different solvents depending on the halide: DMSO/DMF (1:1, v/v) for Cl, DMF for Br, and GBL for I. The precursor solutions were kept with stirring for 1 day and filtered with a 0.2 μm PTFE syringe filter to obtain a clear solution. Organic lead halide perovskite single crystals were formed by keeping the filtered solution for 1 day at different temperatures: 60 °C for Cl, 80 °C for Br, and 110 °C for I. Crystals were washed with copious amounts of hexane to remove the residual solution on the surface and dried under vacuum for 1 day. The x-ray diffraction patterns to evaluate the quality of the samples are displayed in the supplemental material (Fig. S3) [26].

B. Photoluminescence setup

For temperature-dependent PL measurements, a closed-cycle refrigerator was used to control the temperature in the range of 300–5 K. A 50-cm-long spectrograph equipped with a liquid-nitrogen-cooled charge-coupled device (CCD) was used. HeCd laser lines at 325 and 442 nm were used for the excitation of $MAPbCl_3$ and $MAPbBr_3$, respectively, and a 532 nm ND-YAG laser was used for $MAPbI_3$ excitation. For magnetic-field-dependent PL measurements, we used a capacitor-driven pulsed magnet located at the University of Tokyo and a cryogen-free 19 T superconducting dc magnet located at Tohoku University (Fig. S1). The maximum field strength and transient time of the pulsed magnet were up to 60 T and ~35 ms (supplemental material, Fig. S2) [26], respectively. For PL measurements in pulsed magnetic fields, an electron magnifying CCD (EMCCD) was employed to take PL spectra every 400 μs by using the spectra-kinetics acquisition mode during a field pulse. For polarization-dependent PL measurements, a thin plastic circular polarizer was inserted between the optical fiber and the sample. By simply reversing the magnetic-field direction, the PL transition of the reverse spin orientation can be detected without changing the sample alignment. To maintain a constant sample temperature (4.2 K) from eddy-current heating during the transient magnetic pulse, the bottom part of the PL measurement probe (sample mount) was made by nonmetallic components.

III. RESULTS AND DISCUSSION

A. Photoluminescence spectra of $MAPbX_3$

Figure 1 displays the PL spectra of (a) $MAPbCl_3$, (b) $MAPbBr_3$, and (c) $MAPbI_3$ crystals at temperatures varying from 10 to 150 K in steps of 10 K. All samples show band-edge FX transitions indicated by arrows and bound exciton (BX) transitions [27–29]. Both FX and BX transitions exhibit blueshifts as the temperature drops from 150 to ~50 K; with a further drop in temperature, they exhibit redshifts. The redshift below 50 K is typical of excitons and caused by the increase of binding energy with decreasing temperature.

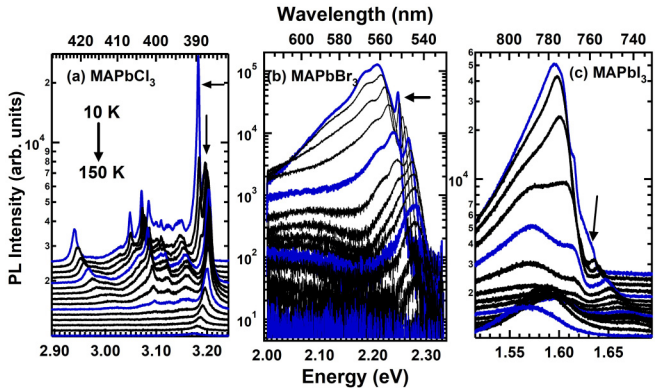

FIG. 1. Temperature dependence of the PL transition spectra of (a) $MAPbCl_3$, (b) $MAPbBr_3$, and (c) $MAPbI_3$ single crystals in steps of 10 K from 10 to 150 K. Arrows indicate FX transitions. In this temperature range (<150 K), all samples were transformed to an orthorhombic structure.

The FX transition intensity changes sensitively with varying external excitation power [28].

Figure 2 shows PL spectra taken under different magnetic fields. Because the transitions of $MAPbCl_3$ in Fig. 2(a) are in the near UV region, only unpolarized spectra can be obtained. At 0 T, $MAPbCl_3$ shows two FX transitions marked as 1 and 2 that undergo spectral redshifts in magnetic fields. Under high magnetic fields above 20 T, a new transition indicated by 3 emerges between the two FX transitions; this transition shows a blueshift with a further increase in the magnetic field. Other sharp peaks in the lower-energy side of the FXs, which are believed to be impurity-related transitions, show redshifts under magnetic fields. For the other two samples, $MAPbBr_3$ (b) and $MAPbI_3$ (c), we obtained circularly polarized PL spectra under magnetic fields, and both show blueshifts. We confirmed that up to 50 T, the linearly polarized PL spectra for these samples did not show any appreciable difference between the longitudinal and transverse directions (see Fig. S4

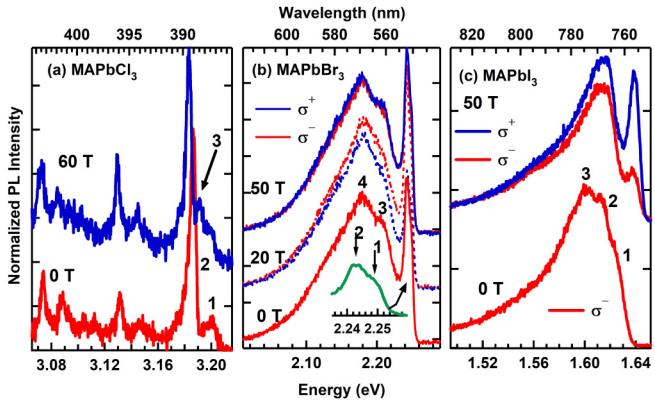

FIG. 2. PL spectra under magnetic fields. (a) For $MAPbCl_3$, two FX transitions labeled as peaks 1 and 2 show redshifts, whereas peak 3 emerged above 20 T and exhibits a blueshift. (b) For $MAPbBr_3$, two FX transitions, labeled peaks 1 and 2, with bound excitons (3 and 4) show blueshifts between 0 to 50 T. (c) For $MAPbI_3$, the FX transition appeared as a small side peak labeled as peak 1 at $B = 0$ T, which notably changed in intensity under magnetic fields.

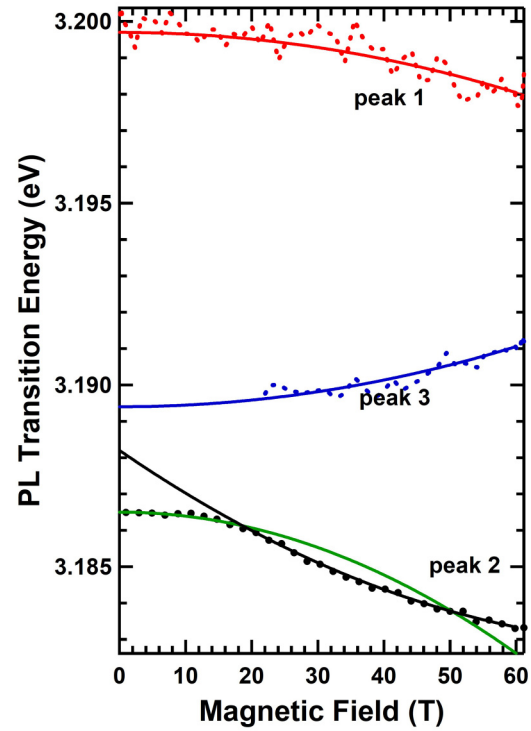

FIG. 3. PL transition-energy shift of three FX transitions from the $MAPbCl_3$ crystal (broken lines). Peaks 1 and 2 show redshifts, whereas peak 3, which emerged above 20 T, exhibits a blueshift. Peaks 1 and 3 fit with $\pm c_0 B^2$, and the fits are shown as red and blue solid lines, respectively. Peak 2 follows $-B^2$ fitting below 20 T; above 20 T, it follows the fitting equation $-\frac{1}{2}\Delta g \mu_B B + c_0 B^2$.

in the supplemental material [26]). In Fig. 2(b), $MAPbBr_3$ shows two energetically closely located FX transitions indicated by vertical arrows with peaks 1 and 2 in the inset of Fig. 2(b). The PL doublet spectrum is reported in most research groups [29–34], wherein the energy separation between two peaks varies from ~123 to ~11 meV. Among them, the result of the Tilchin group with an energy difference of 11 meV between the two peaks at 10 K [29] tends to be consistent with our experimental result with an energy difference of 8 meV at 4.2 K. They claim that these energetically closely located two peaks are associated with $n = 1$ and 2 exciton states. Broad peaks numbered 3 and 4 in Fig. 2(b) are BXs [29]. Unlike $MAPbCl_3$ and $MAPbBr_3$, as shown in Fig. 2(c), $MAPbI_3$ exhibits a single FX transition (peak 1) with two BX transitions (peaks 2 and 3) [28]. In this case, the FX transition shows remarkable changes with increasing magnetic fields for both σ^+ and σ^- directions.

B. Transition energy of $MAPbCl_3$ in magnetic fields

Figure 3 shows the PL transition-energy shifts (ΔE) of excitons under varying magnetic fields. The transition-energy shift ΔE of excitons under magnetic fields can be described as follows:

$$\Delta E = \pm\tfrac{1}{2}\Delta g \mu_B B + c_0 B^2. \quad (2)$$

The first term on the right side of Eq. (2) is the Zeeman energy, wherein Δg is the difference between the electron

and hole g-factors (effective g-factor, hereafter) and μ_B is the Bohr magneton. The second term is the diamagnetic shift with the diamagnetic coefficient $c_0 = e^2 a_B^{*2}/8\mu$, where e is the electric charge, a_B^* is the exciton Bohr radius, and μ is the exciton effective reduced mass. As shown in Fig. 3, the fitting for peak 1 (red solid line) exhibits a negative diamagnetic coefficient of $c_0 = -0.50 \pm 0.034\ \mu\text{eV/T}^2$ without the Zeeman term. Similarly, peak 3, which emerges above 20 T, has a positive sign with the same diamagnetic coefficient, $c_0 = +0.50 \pm 0.028\ \mu\text{eV/T}^2$ (blue solid line). Peak 2 shows a different behavior from peaks 1 and 2. From 0 to ~20 T it decreases slowly, and then it decreases rapidly with a further increase in the magnetic fields. To analyze the PL energy shift of peak 2, we divide the fitting range into the ranges below and above 20 T. Between 0 and 20 T, the fitting follows $\Delta E = -1.08 \times 10^{-6} B^2$ (green solid line). Above 20 T, the fitting follows $\Delta E = -(0.044)\frac{1}{2}\mu_B B + 0.72 \times 10^{-6} B^2$ (black solid line). Therefore, the diamagnetic coefficient of peak 2 changes its sign from negative ($c_0 = -1.08 \pm 0.17\ \mu\text{eV/T}^2$) to positive ($c_0 = +0.72 \pm 0.06\ \mu\text{eV/T}^2$) as the magnetic field increases beyond 20 T. This change in sign indicates that the effective reduced mass has also changed from negative to positive. To understand this peculiar behavior of effective mass, one must consider an effective-mass correction caused by the polaronic and SOI effects. The formation of polarons induced by the electron-phonon interaction decreases the electron energy by the polaron binding energy. In the effective-mass approximation, the reduction of the electron energy increases the effective mass. Consequently, the effective mass of the polaron is greater than that of the band electron. In addition to the polaron effect, the SOI effect modifies the effective mass. The two-dimensional (2D) expression for the polaron effective mass due to Rashba splitting at $k = 0$ can be expressed as follows [35]:

$$\frac{1}{m_{xx}^*} = \frac{1}{m^*} \pm \frac{\alpha k_y^2}{k^3}, \tag{3}$$

where m_{xx}^* is the polaron effective mass and α is the Rashba coupling constant. Although Eq. (3) is estimated for a 2D semiconductor, this equation can be applied to three-dimensional crystals in the presence of a magnetic field because the electron motion in the z-direction (parallel to the magnetic field) carries the linear momentum, and the circular motion is limited in the xy plane. Due to the second term on the right side of Eq. (3), the effective mass of the negative spin can be negative under the strong SOI. Therefore, the negative diamagnetic coefficients of peaks 1 and 2 (below 20 T) are associated with polarons in the negative-spin Rashba band.

When the cyclotron frequency becomes higher than the polaron frequency, carrier motion decouples from the polar lattice [8]. The cyclotron (ω_c) and polaron (ω_p) frequencies [36] are given by

$$r_c = \left(\frac{\hbar^2/2m^*}{\hbar^2\omega_c}\right)^{1/2} = \frac{\ell_B}{\sqrt{2}}, \tag{4}$$

$$r_p = \left(\frac{\hbar^2/2m^*}{\hbar^2\omega_p}\right)^{1/2}, \tag{5}$$

$$\frac{\omega_c}{\omega_p} = \left(\frac{r_p}{r_c}\right)^2 = 2\left(\frac{r_p}{\ell_B}\right)^2, \tag{6}$$

where r_c (r_p) is the cyclotron (polaron) radius and $\ell_B = \sqrt{\hbar/eB} = \sqrt{2}r_c$ is the magnetic length. A comparison of the cyclotron and polaron frequencies indicates that carrier motion decouples from the polar lattice when the magnetic length ℓ_B is comparable to the polaron radius. At 20 T, the cyclotron radius $r_c = 4.0$ nm ($\ell_B = 5.7$ nm), which is close to the radius of the large polaron in $MAPbCl_3$ [37]. Therefore, at approximately 20 T, the polaron effect can be softened. The Zeeman effect gradually increases the transition energy with increasing external magnetic fields, whereas the SOI-induced Rashba effect is constant in external magnetic fields. Therefore, the Rashba effect dominates the Zeeman effect under low magnetic fields, and vice versa under high magnetic fields [38–40]. As a consequence of the softened polaron and Rashba effects, the slope of the peak-2 transition changes, and the effective mass changes from negative to positive as the magnetic field increases beyond 20 T. The energy-shift slope of peak 1 does not change, and the negative effective mass is maintained in the entire field range up to 60 T. The magnetic length at 60 T is $\ell_B = 3.3$ nm, which is not small enough to decouple the electron from the polar lattice in the case of a small polaron that is confined within a unit cell with the lattice constant $a = 5.67$ Å for $MAPbCl_3$. Therefore, the peak-1 and peak-3 transitions are associated with small polarons in the negative and positive spin Rashba bands, respectively. Although the self-trapped small polaron is difficult to form in 3D OIHP materials, our MPL transition suggests that the formation of the small polaron is possible in the $MAPbCl_3$ crystal because of the large ionic bonding ratio and small lattice constant.

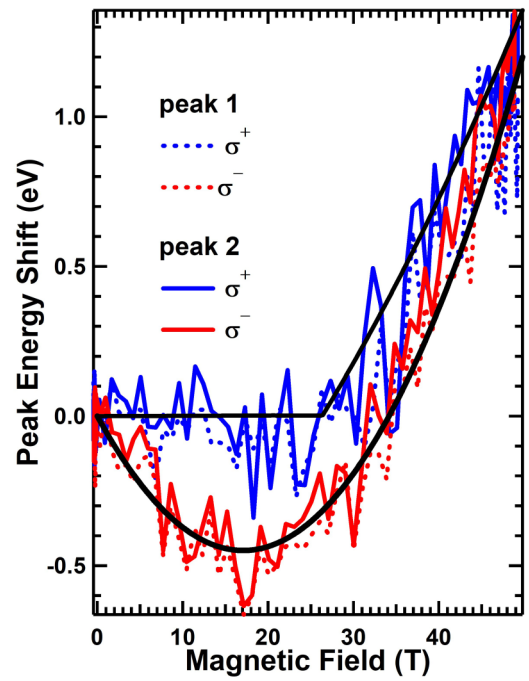

FIG. 4. Two FX transition-energy shifts of the $MAPbBr_3$ crystal in different spin directions. Blue broken (peak 1) and solid (peak 2) lines are from σ^+ transitions, and red broken (peak 1) and solid (peak 2) lines are associated with σ^- transitions. The energy shifts of peaks 1 and 2 in the same direction are almost equal. Black solid lines are fitting lines. A straight line for σ^+ below 28 T is a guide for the eye.

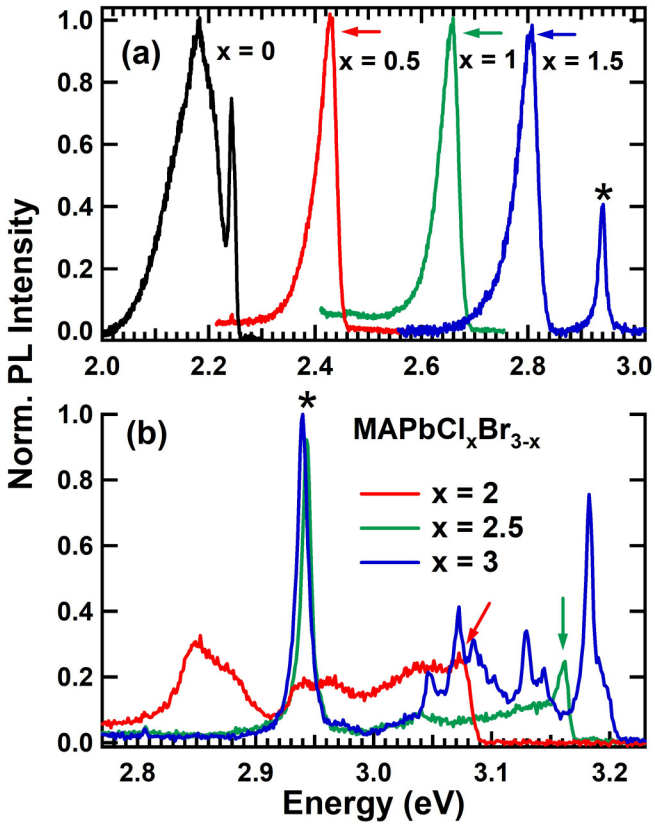

FIG. 5. PL spectra of MAPBCl$_x$Br$_{3-x}$ at $B = 0$ T, 4.2 K. (a) $x =$ 0, 0.5, 1, 1.5 and (b) $x = 2$, 2.5, 3.

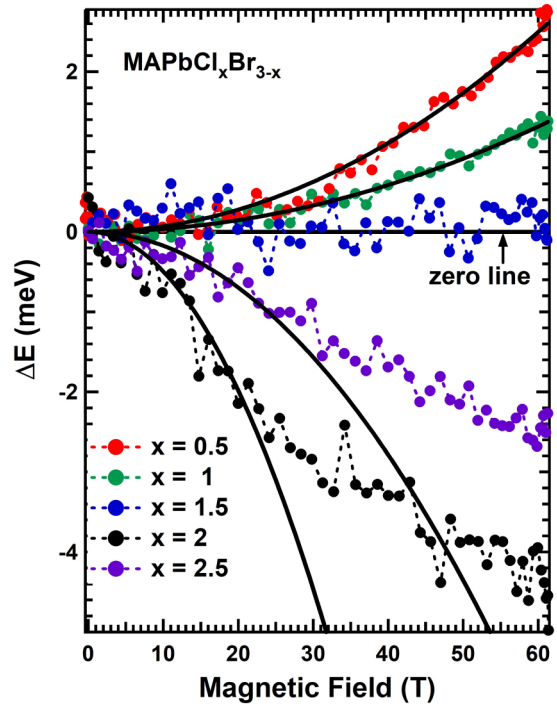

FIG. 6. Estimated peak transition energy in magnetic fields for $x = 0.5$–2.5 indicated by arrows in Fig. 5. Two samples, $x = 0.5$ (red) and 1.0 (green), follow the diamagnetic fitting equation $\Delta E = c_0 B^2$ (black solid lines). For $x = 1.5$ (blue), the peak transition energy barely moves. When x exceeds 2, the diamagnetic energy shift becomes negative (black and purple).

C. Transition energy of $MAPbBr_3$ in magnetic fields

For the $MAPbBr_3$ peak transition energies in Fig. 4, broken and solid lines correspond to the PL transition-energy shifts of peaks 1 and 2 from Fig. 2(b) (inset), respectively, and blue and red indicate σ^+ and σ^- from Fig. 2(b), respectively. Because the electronegativity of Br is smaller than that of Cl, the polaronic effect of $MAPbBr_3$ is weaker than that of $MAPbCl_3$. Consequently, the PL transition behavior of $MAPbBr_3$ is expected to be different from that of $MAPbCl_3$. The total transition-energy shifts in the magnetic fields of two FX transitions are almost identical in the same polarization directions. σ^- transitions (red solid and broken lines) follow Eq. (2) with $\Delta g = -1.82$ and $c_0 = +1.54 \pm 0.045$ μeV/T^2. These values deviate slightly from the result previously published by Tanaka *et al.* [21], who reported these values as $\Delta g = \pm 2.03$ and $c_0 = +1.28$ μeV/T^2 from magnetoabsorption experiments. However, in the opposite spin direction (σ^+), the PL transition-energy shifts for peaks 1 and 2 do not move in magnetic fields below ~30 T. Above 30 T, the shifts fit Eq. (2) with $\Delta g = +0.78$ and $c_0 = +0.46 \pm 0.07$ μeV/T^2, which are significantly smaller than those for the opposite (σ^-) direction. The difference between the different polarization directions may be due to the effective-mass corrections indicated in Eq. (3). Under low magnetic fields, both the Rashba and polaron effects are dominant. However, with increasing magnetic fields, the Zeeman energy becomes more important than the Rashba effect, and the cyclotron frequency is comparable to the polaron frequency. Therefore, under high magnetic fields, both the Rashba and polaron effects are suppressed and the cyclotron motion becomes predominant above 30 T.

D. Transition energy of MAPbCl$_x$Br$_{3-x}$ in magnetic fields

Because the difference of the PL spectral shapes between $MAPbCl_3$ and $MAPbBr_3$ is large [see Figs. 1(a) and 1(b)], we attempted to measure unpolarized PL measurements for MAPbCl$_x$Br$_{3-x}$ ($x = 0.5$–2.5) crystals in magnetic fields. As seen in Fig. 5(a), for $x = 0.5$–1.5, PL spectral shapes are similar to $MAPbBr_3$, whereas for $x = 2$ and 2.5 in Fig. 5(b), spectral shapes are similar to $MAPbCl_3$. When $x \geqslant 1.5$, there is a common peak that appeared at ~2.93 eV marked by asterisks, which can be a bound exciton associated with Cl.

In the presence of magnetic field in Fig. 6, $x = 0.5$ and (red markers) and 1.0 (green markers) exhibit a typical diamagnetic energy shift, $\Delta E = c_0 B^2$ with the diamagnetic coefficients $c_0 = 0.690 \pm 0.010$ and 0.370 ± 0.007 μeV/T^2 for $x = 0.5$ and 1.0, respectively. For the case of $x = 1.5$, the peak energy does not move (see the zero line). With further increasing x, the diamagnetic energy shift becomes negative. Below 20 T, both peak transition energies fit well with the diamagnetic coefficients $c_0 = -4.959 \pm 0.30$ and -1.741 ± 0.19 μeV/T^2 for $x = 2.0$ and 2.5, respectively (see the black solid lines). Comparing not only for spectral shapes but also energy shifts in magnetic fields, when x is smaller or greater than 1.5, the PL transition characteristics become $MAPbBr_3$-like or $MAPbCl_3$-like behavior, respectively.

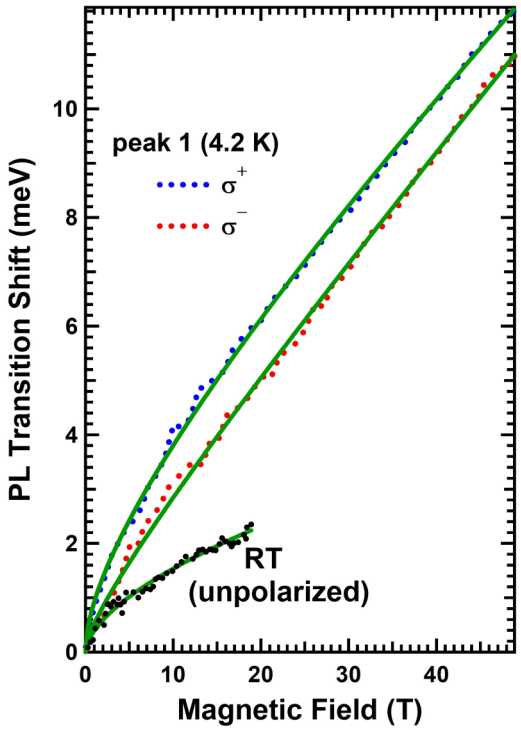

FIG. 7. FX transition-energy shift of the $MAPbI_3$ crystal in different spin directions. Blue and red and broken lines are associated with σ^+ and σ^- transitions, respectively. Both peaks show a power dependency ($\Delta E = aB + bB^m$, where a and b are fitting parameters). A transition at room temperature (black dotted lines), measured under a magnetic field of 19 T produced by a superconducting magnet, also follows the same fitting equation (black solid line).

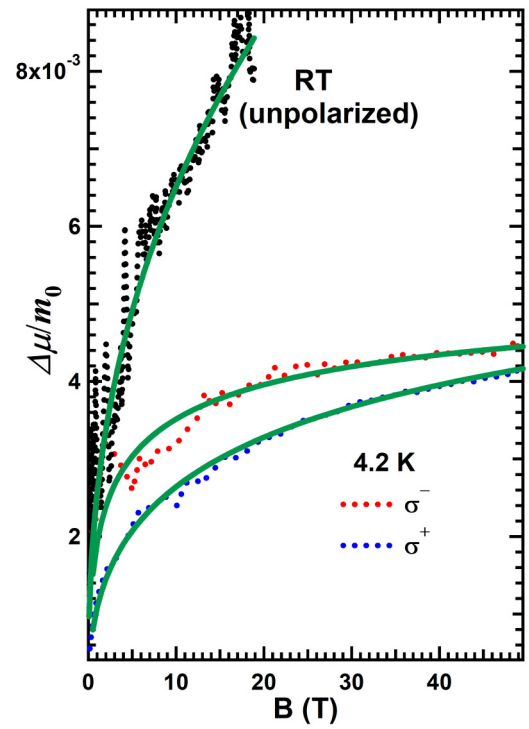

FIG. 8. Estimated change in effective reduced mass [$\Delta\mu^*(B)$] under magnetic fields in units of the electron rest mass (m_0). The nonlinear MPL transition is due to the change in the magnetic-field-dependent effective reduced mass.

E. Transition energy of $MAPbI_3$ in magnetic fields

Iodine has the smallest electronegativity among the halogens used in this study. Therefore, its polaronic effect might be limited in comparison with other elements. The PL transition-energy shifts of $MAPbI_3$ exhibit a completely different behavior from those of the other samples, as shown in Fig. 7. Neither of the $\sigma^{\pm}$ transitions fit Eq. (2), and both exhibit $\Delta E = aB + bB^m$ dependency. In the figure, green lines indicate the fitted values; for σ^+, $a(\sigma^+) = 0.1270 \pm 0.0128$, $b(\sigma^+) = 0.79537 \pm 0.0341$, and $m(\sigma^+) = 0.50328 \pm 0.0373$; and for σ^-, $a(\sigma^-) = 0.17591 \pm 0.0157$, $b(\sigma^-) = 0.34397 \pm 0.0437$, and $m(\sigma^-) = 0.49854 \pm 0.109$. Considering the power m, which is close to 0.5, both polarizations follow $\sqrt{B}$ under low magnetic fields below 20 T and are linear in B under high magnetic fields above 20 T. Furthermore, the room-temperature MPL transition behavior shows the same $\sqrt{B}$ behavior below 20 T. Such a nonlinear energy transition under low magnetic fields may be due to the band nonparabolicity combined with the polaron effect [41–43]. Peeters *et al.* [42] reported that the nonlinear transition occurs at the anticrossing region of the $(n+1)$th zero-phonon and nth Landau level. The LO phonon energy in $MAPbI_3$ is known to be ~35 eV; in our case, the total transition energy between 0 and 50 T is approximately 12 meV. Therefore, the anticrossing between the zero-phonon and no-phonon scenarios does not meet our case.

As chlorine is substituted with iodine, the energy gap decreases, and thus the band-gap nonparabolicity becomes important. For a nonparabolic band, the polaron effective reduced mass (μ) is no longer a constant value; rather, it is a function of the magnetic field [44]:

$$\Delta\mu^*(B) = \frac{\hbar eB}{\Delta E}, \tag{7}$$

where $\Delta\mu^*(B)$ and ΔE are the changes of effective reduced mass and the energy shift in magnetic fields, respectively. Figure 8 shows the change in effective reduced mass under magnetic fields based on Eq. (7) in units of the electron rest mass (m_0), where broken lines indicate experimental values and green solid lines indicate fitted values. For the low-temperature transitions at 4.2 K, the reduced effective mass increases rapidly below 20 T as the MPL transition energies increase rapidly, as shown in Fig. 7. In the high-field region above 20 T, the change in slope of the effective reduced mass becomes low and shows saturation behavior, and the transition energies are linear in B. At room temperature, the effective reduced mass is larger than that at low temperatures (black dotted markers). This temperature dependence of the change in effective reduced mass may be due to the difference in lattice structures between room temperature and 4.2 K.

IV. CONCLUSION

In conclusion, we obtained MPL spectra from $MAPbX_3$ (X = Cl, Br, and I) under strong magnetic fields of up to

60 T by using pulsed magnets. Because the halide changes the MPL transitions in an inconsistent manner, we could not find a unified model to explain the MPL transition-energy behaviors. For $MAPbCl_3$ crystal, two MPL transition peaks follow B^2 behavior up to 60 T at 4.2 K. These transitions are attributed to small polaron transitions. One transition peak energy shows a quadratic dependency on B with a negative sign below 20 T and then follows a normal diamagnetic shift above 20 T. This behavior can be understood as a combination of the Rashba and the large polaron effects, which cause a negative effective reduced mass at low fields below 20 T. The large polaron decouples when the cyclotron frequency becomes comparable to the polaron frequency with increasing magnetic fields above 20 T. For $MAPbBr_3$ crystal, the MPL transition-energy behavior follows a normal diamagnetic shift. However, the coefficients are different from previously reported values obtained using magnetoabsorption measurements. This is because the MPL transition may reflect the polaron effect, whereas the magneto-optical absorption is solely associated with the band-edge transition. For $MAPbCl_xBr_{3-x}$ samples, when $x \leqslant 1.5$ or $x \geqslant 2.0$, the PL transition characteristics are similar to $MAPbBr_x$ or $MAPbCl_3$, respectively.

The power-law dependency of the MPL transition energies for $MAPbI_3$ under magnetic fields is associated with the band nonparabolicity. Because of the nonparabolic band effect combined with the polaron effect, the effective reduced mass changes with the magnetic field. Consequently, by replacing the halogen in OIHP crystals, it is not possible to explain the MPL transition behavior in a unified model, and one must consider different effects with different halogens in OIHP materials. Further detailed insights into such effects have remained for future quantitative theoretical works.

ACKNOWLEDGMENTS

The work at Dankook University is supported by the National Research Foundation of Korea (NRF-2016R1D1A1B01006437) funded by the Korea government (MSIT). The research conducted at Hanyang University is supported by the National Research Foundation of Korea (NRF-2019M3D1A1078304) funded by the Ministry of Science and ICT. A part of this work has been supported by ICC-IMR and the GIMRT program of IMR, Tohoku University and the visiting professor program of ISSP, The University of Tokyo.

[1] National Renewable Energy Laboratory Best Research-Cell Efficiency Chart, https://www.nrel.gov/pv/assets/pdfs/best-research-cell-efficiencies.20200104.pdf (accessed on February 2021).
[2] M. Jeong, I. W. Choi, E. M. Go, Y. Cho, M. Kim, B. Lee, S. Jeong, Y. Jo, H. W. Choi, J. Lee, J.-H. Bae, S. K. Kwak, D. S. Kim, and C. Yang, Science **369**, 1615 (2020).
[3] Z. G. Yu, Sci. Rep. **6**, 28576 (2016).
[4] D. Canneson, E. V. Shornikova, D. R. Yakovlev, T. Rogge, A. A. Mitioglu, M. V. Ballottin, P. C. M. Christianen, E. Lhuillier, M. Bayer, and L. Biadala, Nano Lett. **17**, 6177 (2017).
[5] M. A. Becker, R. Vaxenburg, G. Nedelcu, P. C. Sercel, A. Shabaev, M. J. Mehl, J. G. Michopoulos, S. G. Lambrakos, N. Bernstein, J. L. Lyons, T. Stöferle1, R. F. Mahrt, M. V. Kovalenko, D. J. Norris, G. Rainò, and A. L. Efros, Nature (London) **553**, 189 (2018).
[6] M. Isarov, L. Z. Tan, M. I. Bodnarchuk, M. V. Kovalenko, A. M. Rappe, and E. Lifshitz, Nano Lett. **17**, 5020 (2017).
[7] H. Ryu, D. Y. Park, K. M. McCall, H. R. Byun, Y. Lee, T. J. Kim, M. S. Jeong, J. Kim, M. G. Kanatzidis, and J. I. Jang, J. Am. Chem. Soc. **142**, 21059 (2020).
[8] M. Baranowski and P. Plochocka, Adv. Energy Mater. **10**, 1903659 (2020).
[9] D. Meggiolaro, F. Ambrosio, E. Mosconi, A. Mahata, and F. De Angelis, Adv. Energy Mater. **10**, 1902748 (2020).
[10] D. Ghosh, E. Welch, A. J. Neukirch, A. Zakhidov, and S. Tretiak, J. Phys. Chem. Lett. **11**, 3271 (2020).
[11] A. R. S. Kandada and C. Silva, J. Phys. Chem. Lett. **11**, 3173 (2020).
[12] A. J. Neukirch, W. Nie, J. C. Blancon, K. Appavoo, H. Tsai, M. Y. Sfeir, C. Katan, L. Pedesseau, J. Even, J. J. Crochet, G. Gupta, A. D. Mohite, and S. Tretiak, Nano Lett. **16**, 3809 (2016).
[13] M. Park, A. J. Neukirch, S. E. Reyes-Lillo, M. Lai, S. R. Ellis, D. Dietze, J. B. Neaton, P. Yang, S. Tretiak, and R. A. Mathies, Nat. Commun. **9**, 2525 (2018).
[14] E. Menéndez-Proupin, C. L. B. Beltrán Ríos, and P. Wahnón, Phys. Status Solidi RRL **9**, 559 (2015).
[15] X.-Y. Zhu and V. Podzorov, J. Phys. Chem. Lett. **6**, 4758 (2015).
[16] A. M. Soufiani, F. Huang, P. Reece, R. Sheng, A. Ho-Baillie, and M. A. Green, Appl. Phys. Lett. **107**, 231902 (2015).
[17] K. Miyata, D. Meggiolaro, M. T. Trinh, P. P. Joshi, E. Mosconi, S. C. Jones, F. De Angelis, and X.-Y. Zhu, Sci. Adv. **3**, e1701217 (2017).
[18] R. G. Niemann, A. G. Kontos, D. Palles, E. I. Kamitsos, A. Kaltzoglou, F. Brivio, P. Falaras, and P. J. Cameron, J. Phys. Chem. C **120**, 2509 (2016).
[19] T. Glaser, C. Müller, M. Sendner, C. Krekeler, O. E. Semonin, T. D. Hull, O. Yaffe, J. S. Owen, W. Kowalsky, A. Pucci, and R. Lovrinćić, J. Phys. Chem. Lett. **6**, 2913 (2015).
[20] M. Hirasawa, T. Ishihara, T. Goto, K. Uchida, and N. Miura, Physica B **201**, 427 (1994).
[21] K. Tanaka, T. Takahashi, T. Ban, T. Kondo, K. Uchida, and N. Miura, Solid State Commun. **127**, 619 (2003).
[22] K. Galkowski, A. Mitioglu, A. Miyata, P. Plochocka, O. Portugall, G. E. Eperon, J. T.-W. Wang, T. Stergiopoulos, S. D. Stranks, H. J. Snaith, and R. J. Nicholas, Energy Environ. Sci. **9**, 962 (2016).
[23] A. Miyata, A. Mitioglu, P. Plochocka, O. Portugall, J. T.-W. Wang, S. D. Stranks, H. J. Snaith, and R. J. Nicholas, Nat. Phys. **11**, 582 (2015).
[24] G. Maculan, A. D. Sheikh, A. L. Abdelhady, M. I. Saidaminov, Md. A. Haque, B. Murali, E. Alarousu, O. F. Mohammed, T. Wu, and O. M. Bakr, J. Phys. Chem. Lett. **6**, 3781 (2015).

[25] M. I. Saidaminov, A. L. Abdelhady, B. Murali, E. Alarousu, V. M. Burlakov, W. Peng, I. Dursun, L. Wang, Y. He, G. Maculan, A. Goriely, T. Wu, O. F. Mohammed, and O. M. Bakr, Nat. Commun. **6**, 7586 (2015).

[26] See Supplemental Material at http://link.aps.org/supplemental/10.1103/PhysRevB.104.035205 for the experimental setup, pulsed magnetic field profiles, room-temperature XRD patterns for samples, and linearly polarized MPL spectra, polarization rate, integrated PL intensity, and FWHM in magnetic fields. It contains the following references: J. Ding, H. Fang, Z. Lian, J Li, Q. Lv, L. Wang, J.-L. Sun, and Q. Yan, CrystEngComm **18**, 4405 (2016); G. R. Kumar, A. D. Savariraj, S. N. Karthick, S. Selvam, B. Balamuralitharan, H.-J. Kim, K. K. Viswanathan, M. Vijaykumar, and K. Prabakar, Phys. Chem. Chem. Phys. **18**, 7284 (2016); H. Shen, R. Nan, Z. Jian, and X. Li, J. Mater. Sci. **54**, 11596 (2019); R. Comin, G. Walters, E. Sol Thibau, O. Voznyy, Z.-H. Lu, and E. H. Sargent, J. Mater. Chem. C **3**, 8839 (2015).

[27] L. Q. Phuong, Y. Nakaike, A. Wakamiya, and Y. Kanemitsu, J. Phys. Chem. Lett. **7**, 4905 (2016).

[28] H.-J. Jo, D. Y. Park, M. G. So, Y. Kim, J. S. Kim, and M. S. Jeong, Curr. Appl. Phys. **19**, 60 (2019).

[29] J. Tilchin, D. N. Dirin, G. I. Maikov, A. Sashchiuk, M. V. Kovalenko, and E. Lifshitz, ACS Nano **10**, 6363 (2016).

[30] D. Priante, I. Dursun, M. S. Alias, D. Shi, V. A. Melnikov, T. K. Ng, O. F. Mohammed, O. M. Bakr, and B. S. Ooi, Appl. Phys. Lett. **106**, 081902 (2015).

[31] K.-H. Wang, L.-C. Li, M. Shellaiah, and K. W. Sun, Sci. Rep. **7**, 13643 (2017)

[32] T. Thu Ha Do, A. Granados del Águila, C. Cui, J. Xing, Z. Ning, and Q. Xiong, Phys. Rev. B **96**, 075308 (2017).

[33] Y. Fang, H. Wei, Q. Dong, and J. Huang, Nat. Commun. **8**, 14417 (2017).

[34] S. Yesudhas, R. Burns, B. Lavina, S. N. Tkachev, J. Sun, C. A. Ullrich, and S. Guha, Phys Rev. Mater. **4**, 105403 (2020).

[35] Z. Li, Z. Ma, A. R. Wright, and C. Zhang, Appl. Phys. Lett. **90**, 112103 (2007).

[36] N. Miura, *Physics of Semiconductors in High Magnetic Fields*, Oxford Science Publications (Oxford University Press, Oxford, 2008).

[37] M. Sendner, P. K. Nayak, D. A. Egger, S. Beck, C. Müller, B. Epding, W. Kowalsky, L. Kronik, H. J. Snaith, A. Pucci, and R. Lovrinčić, Mater. Horiz. **3**, 613 (2016).

[38] M. H. Weiler, Semicond. Semimet. **16**, 119 (1981).

[39] T. Y. Kim, S. Joo, J. Lee, J. H. Suh, S. Cho, S. U. Kim, K. Rhie, J. Hong, and K.-H. Shin, J. Kor. Phys. **54**, 697 (2009).

[40] P. Pfeffer and W. Zawadzki, Phys. Rev. B **68**, 035315 (2003).

[41] D. M. Larsen, Phys. Rev. B **30**, 4595 (1984).

[42] F. M. Peeters and J. T. Devreese, Phys. Rev. B **31**, 3689 (1985).

[43] J. Singleton, R. J. Nicholas, D. C. Rogers, and C. T. B. Foxon, Surf. Sci. **196**, 429 (1988).

[44] E. D. Palik, G. S. Picus, S. Teitler, and R. F. Wallis, Phys. Rev. **122**, 475 (1961).

Correction: A minor typographical error in Eq. (7) has been fixed.